

Effective magnetic correlations in hole-doped graphene nanoflakes

A. Valli¹, A. Amaricci¹, A. Toschi², T. Saha-Dasgupta³, K. Held², and M. Capone¹

¹*Democritos National Simulation Center, Consiglio Nazionale delle Ricerche, Istituto Officina dei Materiali (IOM) and Scuola Internazionale Superiore di Studi Avanzati (SISSA), Via Bonomea 265, 34136 Trieste, Italy*

²*Institute for Solid State Physics, Vienna University of Technology, 1040 Wien, Austria and*

³*S. N. Bose National Centre for Basic Sciences, 70098 Kolkata, India*

(Dated: September 29, 2016)

The magnetic properties of zig-zag graphene nanoflakes (ZGNF) are investigated within the framework of the dynamical mean-field theory. At half-filling and for realistic values of the local interaction, the ZGNF is in a fully compensated antiferromagnetic (AF) state, which is found to be robust against temperature fluctuations. Introducing charge carriers in the AF background drives the ZGNF metallic and stabilizes a magnetic state with a net uncompensated moment at low temperature. The change in magnetism is ascribed to the delocalization of the doped holes in the proximity of the edges, which mediate ferromagnetic correlations between the localized magnetic moments. Depending on the hole concentration, the magnetic transition may display a pronounced hysteresis over a wide range of temperature, indicating the coexistence of magnetic states with different symmetry. This suggests the possibility of achieving the electrostatic control of the magnetic state of ZGNFs to realize a switchable spintronic device.

PACS numbers: 71.27.+a, 73.22.-f, 73.22.Gk

I. INTRODUCTION

Graphene is widely regarded as a promising material for nanoelectronics.¹ The high electron mobility of the delocalized π -electrons in graphene results in excellent electric and thermal transport properties, leading the belief that graphene holds the potential to outperform Si for the realization of high-speed and high-frequency response transistors and large-scale integrated circuits with a low environmental impact. In this respect, the semi-metallic nature of graphene is not ideal for electronic applications, and represents the main limitation to the realization of a graphene transistor. This issue can be overcome when considering nanostructured subunits of graphene: 0D graphene nanoflake (GNFs) and their 1D counterparts, graphene nanoribbons (GNRs) which display a semiconducting gap strongly dependent on the system's size.^{1,2} Particularly interesting is the role of the topology of the edge termination of graphene nanostructures in the stabilization of a magnetic state. Graphene zigzag (ZZ) edges have a defined chirality and consist of atoms belonging to the same triangular sublattice of graphene, while in armchair (AC) edges atoms of both sublattices are always paired. The unbalance at the ZZ edges is believed to be the origin of magnetism. This feature raised the interest for graphene applications also in the field of spintronics.

Recent experimental evidence³⁻⁶ supports the idea that magnetism can be intrinsic in graphene nanostructures, and exceptionally high Néel temperatures up to room temperature have been reported.⁶ In general, the experimental observation of magnetic states in graphene nanostructures remains scarce and controversial, and one of the main difficulties in the realization of long-range magnetic structures reside in the growth and in the in-

trinsic irregularity of the sample edges.⁵ However, in the last few years, we witnessed important advances in the synthesis and in the characterization of graphene nanostructure, e.g., at the interface with boron nitride,^{7,8} and the fingerprints of atomically precise edges have been uniquely identified in the Raman spectra of GNRs,⁹ paving the path toward graphene nanoelectronics.

From the theoretical point of view there is a substantial agreement on the phenomenon of edge magnetism within the framework of density functional theory (DFT)¹⁰⁻¹⁴ and the mean-field approximation of the Hubbard model.^{15,16} In particular, it has been proposed that the magnetic states of graphene nanostructures can be exploited for the realization of spintronic devices, e.g., spin filters^{12,13,17,18} and logic gates^{16,19} with graphene functional blocks. Recent investigation^{14,20} suggested that the magnetic ordering of the ZZ edges in GNF can be tuned by carrier doping. The presence of delocalized charge carriers entails ferromagnetic (FM) correlations, giving rise to a complex magnetic phase diagram. Indeed, it has been shown that the correlations between spatially separated magnetic impurities adsorbed on graphene can be interpreted in terms of a Rudermann-Kasuya-Kittel-Yoshida (RKKY) exchange interaction mediated by the π -electrons of the graphene substrate.²¹⁻²⁵

Besides a few relevant exceptions,^{20,21,26-28} the role of electronic correlations beyond mean-field theory (MFT) in graphene nanostructures remains widely unexplored. This calls for better theoretical understanding, in particular, on the effect of electronic correlations on the magnetic properties and the interplay between the charge and spin degrees of freedom in the presence of ZZ edges. We address this question in the framework of the dynamical mean-field theory (DMFT)²⁹ which is able to describe the interplay between the low-energy coherent excitations, arising due to the delocalization of the charge carriers on

the lattice, and the incoherent high-energy excitations, related to the formation of the fluctuating local moment due to the Coulomb interaction.

The paper is organized as follows. In Sec. II A we discuss the Hubbard model as a generic low-energy model for GNFs, while in Sec. II B and II C we show how DMFT allows to investigate the magnetic properties of GNFs in the presence of electronic correlations. In Sec. III we present our numerical results. We focus on the case of a hexagonal ZGNF and discuss the onset of magnetism at half-filling as well as the interplay between charge and spin degrees of freedom at finite doping. Finally, Sec. IV contains our conclusion and outlook.

II. MODEL & METHODS

A. Low-energy π -electrons Hamiltonian for GNFs

In graphene, the in-plane C-C bonds are formed due to a sp^2 -hybridization between carbon s , p_x , and p_y atomic orbitals, while the p_z orbitals are perpendicular to the sp^2 bonds and bind into π orbitals that extend over the plane. Hence, in order to describe a GNF we can consider the following Hubbard Hamiltonian as an effective low-energy model for the delocalized π -electrons on a finite-size honeycomb lattice with N sites

$$\mathcal{H} = - \sum_{ij\sigma} t_{ij} c_{i\sigma}^\dagger c_{j\sigma} - \mu \sum_{i\sigma} c_{i\sigma}^\dagger c_{i\sigma} + U \sum_i n_{i\uparrow} n_{i\downarrow}. \quad (1)$$

In this notation, the operator $c_{i\sigma}^{(\dagger)}$ annihilates (creates) a π -electron on site i with spin σ and $n_{i\sigma} = c_{i\sigma}^\dagger c_{i\sigma}$ is the corresponding number operator; t_{ij} are the tight-binding hopping parameters, μ is the chemical potential, and U denotes the local Coulomb repulsion.

The information on the spatial arrangement of the C atoms in the nanostructure is contained in the real-space hopping matrix, including also the topology of the edges (either ZZ or AC). Here, we restrict ourselves to consider the case of the hexagonal ZGNF shown in Fig. 1, while spatial symmetries are discussed in detail in Sec. II C. We assume a homogeneous hopping $t_{ij} = t$, where the nearest-neighbor (NN) hopping amplitude $t \equiv 1$ sets the energy scale of the system, and we neglect hopping processes beyond NN. Recently, Kretinin *et al.*³⁰ experimentally estimated the value of the next-NN hopping parameter in graphene to be $t'/t \approx 0.1$. While the presence of t' have important consequences as breaking the particle-hole symmetry of the Hamiltonian, it was concluded that the asymmetry leads to relatively weak effects in the optical, as well as in the electronic, and presumably spin transport properties of monolayer graphene.³⁰ A configuration with spatially uniform hopping parameters is representative of the case where all the dangling C-C bonds at the ZZ edges are passivated, e.g., with hydrogen atoms. Within DFT it was shown that passivation quenches significantly the edge magnetic moments, while the lack

of passivation changes the sp^2 -hybridization between C atoms and induces sizable lattice distortions, mostly at the edges but also in the bulk.¹⁴ A full structure relaxation allows to derive the DFT tight-binding parameters, i.e., the hopping amplitudes and the local crystal fields of the distorted structure. However, according to the numerical results, both neutral and hole-doped case (and in contrast to the electron-doped one) the ZGNF does not display sizable lattice distortions, and the doped charges are distributed symmetrically over the edges.¹⁴ In the following analysis we focus on hole-doped ZGNFs in order to study the interplay between charge and spin degrees of freedom in the stabilization of different magnetic phases. Hence, we disregard the effects of lattice distortions as we do not expect any qualitative change in the results obtained. Finally, we consider a local Coulomb interaction U between the delocalized π -electrons. Recently, both local and non-local Coulomb repulsion terms have been estimated to be sizable in graphene,³¹ justifying the necessity to treat graphene beyond the tight-binding or mean-field approximation. Indeed, electronic correlations, as well as the interplay between local and non-local repulsive interactions are expected to play an important role in the stabilization of different magnetic orders in graphene nanostructures.²⁰ In the following we shall focus on the dynamical correlation effects driven by the local repulsion U within the framework of DMFT.²⁹ Unless specified otherwise, we choose a typical value of $U = 3.75t$, in line with recent estimates for graphene.^{31,32} Non-local interaction could be taken into account within DMFT by including in Hamiltonian (1) a mean-field term $V_{ij} \sum_{\sigma} n_{i\sigma} (\langle n_{j\uparrow} \rangle + \langle n_{j\downarrow} \rangle)$. However, the presence of non-local repulsion favors charge modulation on the lattice and possibly leads to the proliferation of ordered states, which makes this extension beyond the scope of the present work.

B. Real-space dynamical mean-field theory with magnetic symmetry breaking

DMFT is a well established theoretical tool that allows to take into account local electronic correlations non-perturbatively. Numerous extensions of DMFT have also been proposed in which the self-energy is local albeit site-dependent, allowing to deal with inhomogeneous³³⁻³⁶ and nanoscopic³⁷⁻⁴² systems, where in general the translational symmetry is broken along one or more directions in space. Non-local electronic correlations beyond mean-field are in general expected to be important in low-dimensional system. However, by means of comparative studies⁴² with diagrammatic⁴³ extensions of DMFT built on the local two-particle vertex function⁴⁴ it has been demonstrated how a reasonable insights of electronic and transport properties of correlated nanostructures^{37,39,42} are already gained at the DMFT level. In the following we briefly recall how DMFT is implemented for an inhomogeneous finite system, and we discuss how to handle

magnetic phases within this framework. In the case of a finite system, one can map each site $i = 1, \dots, N$ of the original many-body problem onto an auxiliary Anderson impurity model (AIM) embedded in a self-consistent bath determined by the rest of the system. The auxiliary AIM for the i -th site is defined by the spin-dependent local dynamical Weiss field $\mathcal{G}_{0i\sigma}(\omega)$ in terms of the local element of the real-space Green's function $G_{ij\sigma}(\omega)$ of the whole system and the local self-energy $\Sigma_{i\sigma}(\omega)$ as

$$\mathcal{G}_{0i\sigma}^{-1}(\omega) = G_{ii\sigma}^{-1}(\omega) + \Sigma_{i\sigma}(\omega). \quad (2)$$

In general, the local problems defined by $\mathcal{G}_{0i\sigma}^{-1}(\omega)$ are inequivalent, and each of them can be solved numerically yielding a local dynamical self-energy $\Sigma_i(\omega)$ which carries a spatial dependence on the site index i . However, one can exploit any spatial symmetry of the original system and reduce the numerical effort by solving, eventually, only a subset of $N_{\text{ineq}} \leq N$ inequivalent local problems. This reduced the complexity of the problem from exponential in N to linear in N_{ineq} . The knowledge of all (inequivalent) $\Sigma_i(\omega)$ allows to compute the Green's function of the whole system from the real-space Dyson equation

$$G_{ij\sigma}^{-1}(\omega) = (\omega + \mu)\delta_{ij} - t_{ij} - \Sigma_{i\sigma}(\omega)\delta_{ij}, \quad (3)$$

where the self-energy matrix only contains the local, site-dependent elements. Non-local correlations between different sites are neglected. From the Green's function one can define a new set of auxiliary AIMs and iterate the above process self-consistently until convergence.

In order to study the emergence of magnetism, we lift the local $SU(2)$ spin rotational symmetry of the auxiliary AIM, and allow the impurity solver to access solutions with a finite on-site magnetization $\langle S_i^z \rangle = \langle n_{i\uparrow} - n_{i\downarrow} \rangle$ (here we only consider solutions with magnetization in

the z direction). This is done locally for each site i using a symmetry-broken Weiss field $\mathcal{G}_{0i\sigma}$ as initial input for DMFT. In this respect, the separate treatment of the different spin directions is the only essential modification of the general self-consistent scheme of real-space DMFT, and in particular the self-consistent equations, whatever is the magnetic phase to be investigated, as opposed to the standard implementation of symmetry-broken solutions within DMFT.²⁹ The landscape of the possible magnetic phases that can be explored within this approach depends on the set of spatial symmetries enforced in the calculation and on the specific choice of the initial symmetry-breaking.

C. Spatial symmetries and magnetic phases of hexagonal ZGNFs

In the following we discuss in detail the spatial symmetries of hexagonal ZGNFs which we enforce in order to investigate a landscape of possible magnetic configurations within the self-consistent DMFT calculations. We consider the hexagonal ZGNF shown in Fig. 1, which consists of a bipartite honeycomb lattice with $N = 54$ C atoms. Exploiting both the rotational symmetry of the C_{3v} point-group and the sublattice symmetry, one can identify $N_{\text{ineq}} = 6$ inequivalent C atoms all belonging to the same triangular sublattice (e.g., sublattice \mathcal{A}). The inequivalent C atoms can be further distinguished into bulk-atoms (denoted as C_b^{1-4}), which have three in-plane sp^2 C-C bonds, and edge-atoms (denoted as $C_e^{1,2}$), which have two C-C bonds and one dangling/passivated bond. A ZZ edge of the ZGNF consists of $N_{\text{edge}} = 3$ C atoms, i.e., two (equivalent) C_e^1 atoms and a C_e^2 atom, all belonging to the same sublattice. Neighboring edges consist of C atoms belonging to different sublattices, and are always connected by an AC bond between C_e^1 atoms. Lifting the local $SU(2)$ spin rotational symmetry would be enough to study, e.g., (inhomogeneous) FM. However, as the Hubbard model on a bipartite lattice has a natural tendency toward a Néel AF state (close to half-filling), a natural choice would be to enforce each kind of inequivalent atom to have opposite magnetization on different sublattices. However this assumption would not allow other magnetic configurations, and in particular FM. A more general description of the magnetic phases requires instead to raise the number of inequivalent atoms in the system. Here we choose to lift the sublattice symmetry, i.e., treat each inequivalent atom and its counterpart in the other sublattice independently, thus raising $N_{\text{ineq}} : 6 \rightarrow 12$. This choice allows us to stabilize either an AF or a FM state and describe the competition between the two short-range magnetic orders emerging from the interplay between charge and spin degrees of freedom at finite doping.

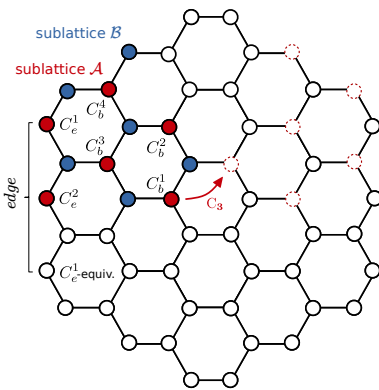


FIG. 1. (Color online) Schematic representation of the hexagonal ZGNF considered. The $N_{\text{ineq}} = 6$ inequivalent C atoms are distinguished into bulk- ($C_b^{1,\dots,4}$) and edge-atoms ($C_e^{1,2}$) for each sublattice \mathcal{A} (red/dark grey) and sublattice \mathcal{B} (cyan/light grey). The rotational symmetry C_3 sends each inequivalent atoms to their equivalent atoms of the same sublattice, indicated with dashed circles.

III. RESULTS AND DISCUSSION

In the following sections we discuss the onset of AF insulating state of a ZGNF at half-filling. We also show that at finite doping there exist another magnetic state underneath the AF one, in which the magnetic moments at the ZZ edges are aligned FM. Such a state is unstable with respect to temperature fluctuations. We discuss its possible origin of the magnetic transition analyzing the effective magnetic exchange interaction mediated by the charge carriers.

A. ZGNF at half-filling

At half-filling, which corresponds to an average occupation of $\langle n \rangle = 1$ electrons/site, and for passivated edges (i.e., in the case of homogeneous hopping parameters), Hamiltonian (1) is particle-hole symmetric and the density of states of the ZGNF is symmetric with respect to the chemical potential. Due to the discreteness of the spectrum, even in the absence of Coulomb interaction the system is semiconducting, with a charge gap $\Delta_0 \approx 0.7t$. The value of Δ_0 depends on the system's size and shape, and in particular it has been shown both experimentally⁴⁵ and theoretically⁴⁶ that it decreases as $1/L$ with the linear size L of the GNF and vanish toward the semimetallic limit realized in bulk graphene.

We characterize the onset of the AF state at half-filling and at $T = 0$ by comparing the results obtained within static mean-field theory (MFT) and DMFT. In the main panel of Fig. 2 we show the local magnetic moment $\langle S_i^z \rangle = \langle n_{i\uparrow} - n_{i\downarrow} \rangle$ for representative atoms in the

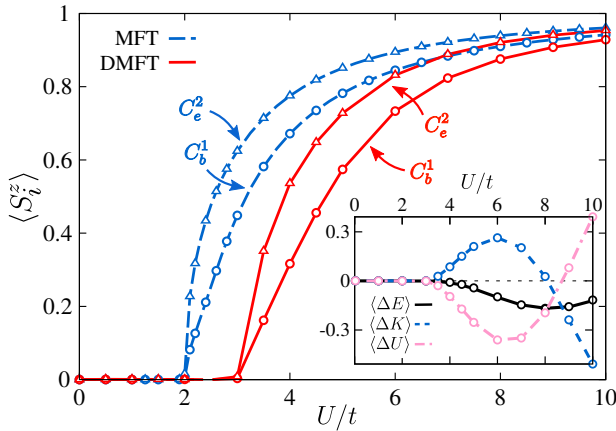


FIG. 2. (Color online) Onset of the AF order at $T = 0$ within static MFT (cyan/light grey) and DMFT (red/dark grey). The local ordered magnetic moment $\langle S_i^z \rangle = \langle n_{i\uparrow} - n_{i\downarrow} \rangle$ for representative bulk C_b^1 and edge C_e^2 atoms displays a clear bulk-edge dichotomy. [Inset] DMFT energy balance between the fully-compensated AF and the PM phases. The total energy difference $\langle \Delta E \rangle = \langle H \rangle_{\text{AF}} - \langle H \rangle_{\text{PM}}$ is separated into kinetic $\langle \Delta K \rangle$ and potential energy $\langle \Delta U \rangle$ contributions.

ZGNF, i.e., for bulk C_b^1 and edge C_e^2 atoms, as a function of the local interaction U/t . It is interesting to notice that the onset of AF happens at a finite value of U/t and simultaneously for all inequivalent atoms, even though the size of the ordered moment of C_b^{1-4} (which are all similar, yet not identical) is different from that of C_e^1 and C_e^2 . Hence, we observe a clear *dichotomy* between bulk and edge atoms, even in the passivated case, which persists also when increasing the interaction. The resulting magnetic state is a fully-compensated AF state but it is different from the conventional Néel state due to the inhomogeneous spatial distribution of the magnetic moments. Both static MFT and DMFT show the qualitative trend discussed above. Unsurprisingly, dynamical quantum effects suppress the AF phase, pushing the onset interaction toward the strong coupling regime, i.e., from the value $U_{\text{AF}} \approx 2t$ obtained within static MFT to the value $U_{\text{AF}} \approx 3t$ obtained within DMFT. Feldner *et al.*²⁶ have shown that static MFT overestimates both the size of the local magnetic moment and the spectral gap of half-filled ZGNFs with respect to exact diagonalization and Quantum Monte Carlo simulations. It is also interesting to notice that the relative difference in size between the magnetic moment of bulk and edge atoms is enhanced within DMFT with respect to static MFT. In fact, the spatial variation of the ordered local moment $\langle S_i^z \rangle$ can be traced back to a preformed (disordered) local moment in the paramagnetic (PM) state $\langle p_i \rangle = \langle (S_i^z)^2 \rangle = \langle n_{i\uparrow} + n_{i\downarrow} \rangle - 2\langle n_{i\uparrow}n_{i\downarrow} \rangle$, which already displays the bulk/edge dichotomy. In the magnetic state the value of $\langle p_i \rangle$ increases due to the decrease of the double occupation $\langle n_{i\uparrow}n_{i\downarrow} \rangle$, as each sites stays locally half-filled, i.e., $\langle n_i \rangle = 1$. In the inset of Fig. 2 we show the DMFT energy balance as a function of U/t , where the internal energy difference between the fully-compensated AF and the paramagnetic phases, i.e., $\langle \Delta E \rangle = \langle H \rangle_{\text{AF}} - \langle H \rangle_{\text{PM}}$ is separated into kinetic $\langle \Delta K \rangle$ and potential energy $\langle \Delta U \rangle$ contributions. For realistic values of the interaction parameter in graphene, the AF state is stabilized by a gain of potential energy $\langle \Delta U \rangle < 0$ corresponding to the reduction of the double occupation upon ordering. The above scenario mirrors the well-known DMFT picture^{47–50} of the AF transition in the bulk Hubbard model, with its crossover from weak-to-strong coupling physics at values of U of the order of the bandwidth. This consideration would put any realistic value of the interaction in ZGNF definitely on the weak-coupling (Slater) side. The main difference here is that the AF phase is not stabilized at arbitrary weak coupling, but it requires a finite onset interaction U_{AF} due to the semiconducting nature of the ZGNF at half-filling. Let us note that the value of the onset interaction depends on the size of the (correlated) spectral gap Δ in the PM phase, which shrinks with the linear size L of the ZGNF.^{45,46} Thus ZGNF with increasing size are expected to become magnetic at weaker interaction, while for small ZGNF the onset interaction U_{AF} is dominated by finite-size effects. Further increasing the

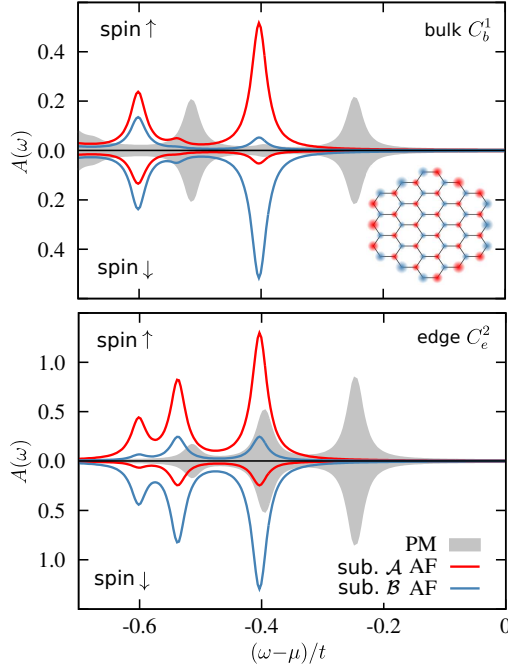


FIG. 3. (Color online) Local spin-resolved DMFT spectral function $A(\omega)$ for bulk C_b^1 (upper panel) and edge C_e^2 (lower panel) atoms at $U/t = 3.75$, $\langle n \rangle = 1$, and $T = 0$. In the non-magnetic calculation the ZGNF is a semiconductor (grey shaded area) while the magnetic calculation yields a fully-compensated AF insulating state, with opposite spin polarization in sublattice \mathcal{A} (red/dark grey solid line) and \mathcal{B} (cyan/light grey solid line). The spatial distribution of the magnetic moments on the ZGNF is represented in the inset, where the color and the radius of the circles indicate the sign and the magnitude of $\langle S_i^z \rangle$.

size the semimetallic nature of graphene plays a role. In fact, despite $\Delta \rightarrow 0$, the lack of perfect nesting on the honeycomb lattice and the zero density of states at the Dirac point keep the onset interaction finite. Theoretical estimates of the onset interaction range from $U_{\text{AF}} \approx 3.8t$ to $U_{\text{AF}} \approx 4.5t$ with different numerical techniques,^{51–54} which seems to be in agreement with the experimental absence of AF in graphene monolayers.

It is interesting to discuss in detail the change in the low-energy spectral properties of the half-filled ZGNF across the magnetic transition. In Fig. 3 we show the occupied portion of the local spin-resolved spectral function $A(\omega < 0)$ for representative bulk C_b^1 and edge C_e^2 atoms. Due to the particle-hole symmetry, the spectral function for spin σ fulfills the relation $A_\sigma(\omega > 0) = A_{\bar{\sigma}}(-\omega)$. We consider a local interaction $U = 3.75t$, which at $T = 0$ lies above but close to the DMFT onset value U_{AF} . In the absence of magnetism, the ZGNF in Fig. 3 is semiconducting, and the local spectral function (grey shaded area) displays a spectral gap $\Delta \approx 0.5t$, where the gap is defined as the distance between the lowest energy peaks around the Fermi level. we notice that the spectral gap Δ is substantially *reduced* by local electronic correlations with

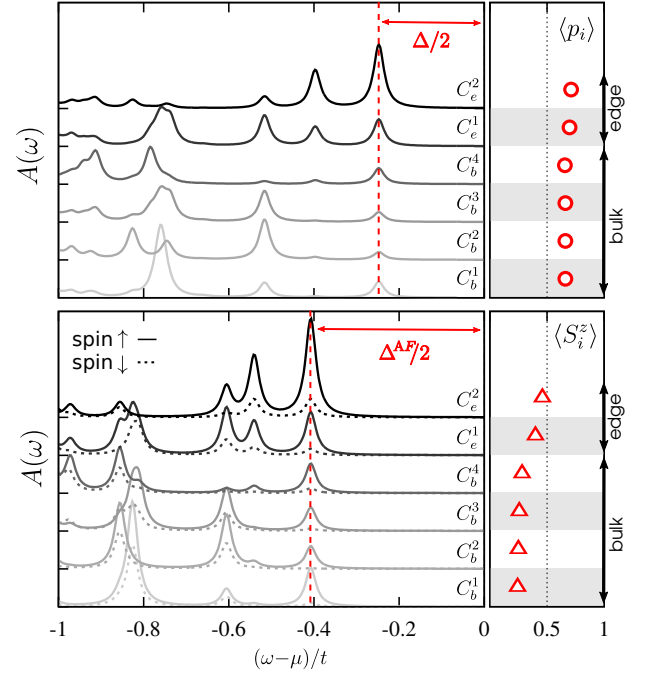


FIG. 4. (Color online) Local spin-resolved DMFT spectral function $A(\omega)$ for all inequivalent C atoms in the PM (upper panel) and AF (lower panel) state at $U/t = 3.75$, $\langle n \rangle = 1$, and $T = 0$. The electronic coherence at low-energy determines homogeneous spectral gaps Δ and Δ^{AF} (vertical dashed lines), despite the disordered $\langle p_i \rangle$ and ordered $\langle S_i^z \rangle$ local moments (open symbols in the side panels) display a clear bulk-edge dichotomy.

respect to the tight-binding value $\Delta_0 \approx 0.7t$, as expected in view of similar observations (within DMFT) in the insulating state of both bulk crystal⁵⁵ and molecules.⁴² In the fully-compensated AF phase we plot $A(\omega)$ for atoms in both sublattices, to show that the spin- \uparrow and spin- \downarrow spectral functions are inverted between the sublattices as a consequence of the particle-hole symmetry, which is fulfilled at half-filling. It is important to notice that both the gap in the PM state Δ and the AF gap Δ^{AF} do not display any spatial dependence over the ZGNF, despite the local magnetic moment of bulk and edge C atoms being different. This is shown in Fig. 4, where we plot the site-resolved spectral functions for all inequivalent atoms of sublattice \mathcal{A} in the PM state (upper panel) and for both spin- \uparrow and spin- \downarrow in the fully-compensated AF state (lower panel). The vertical dashed line indicates the position of the lowest-energy peak for both spin polarizations. The side panels show also the corresponding disordered local moment $\langle p_i \rangle$ and magnetic moment $\langle S_i^z \rangle$. The homogeneity of the spectral gap is the fingerprint of the separation between low-energy delocalized excitations and high-energy localized states in strongly correlated systems. The high-energy properties follow the inhomogeneity dictated by the geometry or the single-particle potential to minimize the potential energy, while the low-energy properties, and in particular

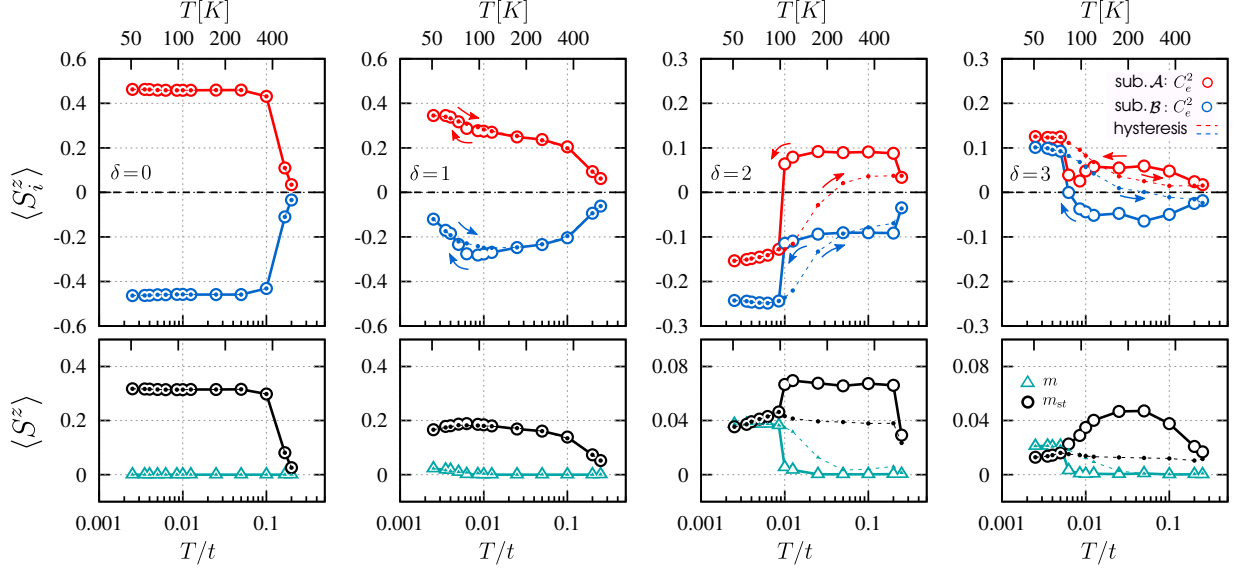


FIG. 5. (Color online) Evolution of the magnetic moments in the ZGNF as a function of temperature T/t at $U/t = 3.75$ and different values of doping δ . As a reference, the temperature scale in K is obtained considering a realistic value $t = 2.7$ eV for the hopping parameter in graphene. [Upper panels] Local magnetic moment $\langle S_i^z \rangle$ for the edge C_e^2 atoms in sublattice \mathcal{A} (red/dark grey symbols) and sublattice \mathcal{B} (cyan/light grey symbols). [Lower panels] Absolute value of the net magnetic moment m (jade/light grey triangles) and the staggered magnetization m_{st} (black circles) per atom in the ZGNF. The dashed line with filled symbols show the hysteretic behavior of the magnetization.

the spectral gap, are more homogeneous as they are associated to a delocalized behavior which lowers the kinetic energy.⁵⁶ In this respect, we can conclude that, for the linear size of the ZGNF that we have considered here, one can observe both the finite-size effects, which result in the physics being dominated by the ZZ edges, but also electronic features that would be expected in the bulk of an infinitely extended system.

Extending the analysis to finite temperature, as also discussed in detail in the following section, we find the fully-compensated AF state at half-filling to be stable up to room- T (see first panel of Fig. 5), in agreement with recent experimental evidence in ZGNRs.⁶ Moreover, the properties of the ordered state, and in particular the local magnetic moments $\langle S_i^z \rangle$ display a very weak dependence on T in the whole range of T explored.

B. Competing magnetic orders upon doping

In the following we explore the interplay between charge and spin degrees of freedom upon hole doping.⁵⁷ Charge carriers can be introduced in the ZGNF, e.g., by using a gate electrode or by chemical substitution with carboxyl (COOH) or hydroxyl (OH) groups, which should not disrupt the sp^2 hybridization at the edges.⁵⁸ The most interesting result is that the fully-compensated AF state is unstable upon doping, due to the emergence of ferromagnetic (FM) correlations between spins at the ZZ edges. We show that at finite doping and below a critical temperature T_c it is energetically favorable for the lo-

cal magnetic moment $\langle S_i^z \rangle$ of the C_e^2 atoms to be aligned FM both within the same edge and between neighboring edges, while bulk C atoms tend to maintain an AF pattern. The resulting magnetic state is characterized by a uncompensated net magnetic moment *and* a finite staggered magnetization. In the following we denote it as ferrimagnetic (FI) state, although we stress that the ZGNF does not display a proper FI ordered. A similar behavior upon doping was recently observed for the same ZGNF within DFT calculations at $T = 0$.¹⁴

The upper panels of Fig. 5 show the temperature evolution of the local magnetic moment $\langle S_i^z \rangle$ for the edge C_e^2 atoms of sublattice \mathcal{A} and \mathcal{B} . We provide also reference values of T in K, obtained with a typical value $t \approx 2.7$ eV for the hopping integral in bulk graphene. The doping is denoted by δ , the integer number of holes in the ZGNF, so that nominal filling of the ZGNF is $n = (N - \delta)/N$. For all the cases we considered, the magnetic state in the high- T is a the fully-compensated AF state. The orientation of the magnetic moment is opposite for atoms in different sublattices, giving rise, globally, to a staggered magnetization $m_{st} = \frac{1}{N} \sum_{i=1}^N \langle S_i^z \rangle^i$. Away from half-filling and below a doping-dependent temperature $T_c(\delta)$ the system also develops a finite net magnetic moment $m = \frac{1}{N} \sum_{i=1}^N \langle S_i^z \rangle$ (uniform magnetization) which coexists with a finite m_{st} giving rise to a FI state. The results for the absolute value of the magnetic moments m and m_{st} are shown in the lower panels of Fig. 5 for each δ . At half-filling the fully-compensated AF state is characterized by a Néel temperature $T_N \approx T_{\text{room}}$ and does not display any tendency toward the FI state down to

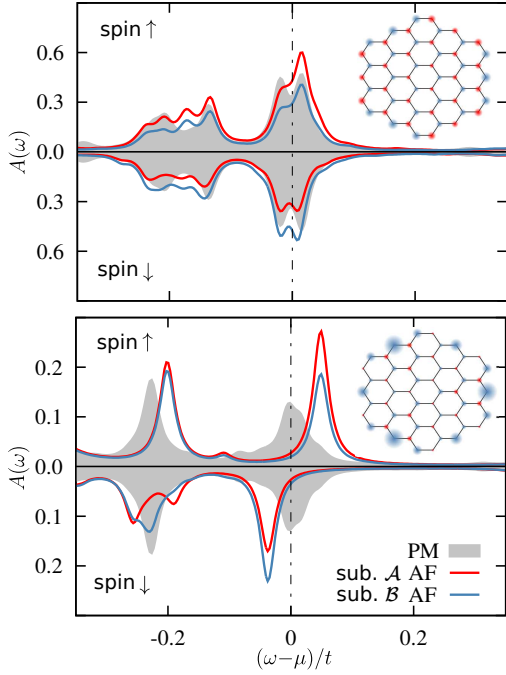


FIG. 6. (Color online) Local spin-resolved DMFT spectral function $A(\omega)$ for the edge C_e^2 atoms at $U/t = 3.75$ and $\delta = 2$. The data are shown for $T \approx 160$ K (upper panel) and $T \approx 80$ K (lower panel) which are representative of the high- T fully-compensated AF state and the low- T FI state, respectively. The color coding reads as in Fig. 3 for both the main panels and the inset.

the lowest T explored. While the mean-field character of the spatial fluctuations within DMFT is known to overestimate the ordering temperature,^{59,60} the observation of a sizable T_N for edge magnetism is in agreement with recent experimental evidence in ZGNR.⁶ The annealing procedure at $\delta \neq 0$ shows that the ZGNF is driven away from a fully-compensated AF state upon lowering T by breaking the spin inversion symmetry between the \mathcal{A} and \mathcal{B} sublattices. In the case of one hole, i.e., $\delta = 1$ (second panel from the left in Fig. 5), the local magnetic moments $\langle S_i^z \rangle$ for the C_e^2 atoms increases, as to be expected, upon lowering T until the sublattice symmetry is broken at $T_c/t \approx 0.008$ ($T_c \approx 100$ K). Below T_c , the staggered magnetization m_{st} decreases and the ZGNF develops a net magnetic moment $m \neq 0$. The major contribution to m (and to the decrease of m_{st}) is given by the asymmetry that develops between the magnetic moments of the C_e^2 atoms in the two sublattices. Let us stress once again that the magnetic transition happens *spontaneously* upon annealing, as the symmetries of the ZGNF enforced in the numerical calculation allow both the AF and the FM solutions, as well as the coexistence of the two orders. The situation is substantially different at higher hole concentrations. At $\delta = 2$ (third panel in Fig. 5) the ZGNF displays a sudden change in the magnetic configuration at $T_c/t \approx 0.02$ ($T_c \approx 140$ K) from a high- T fully-compensated AF state to a low- T FI state.

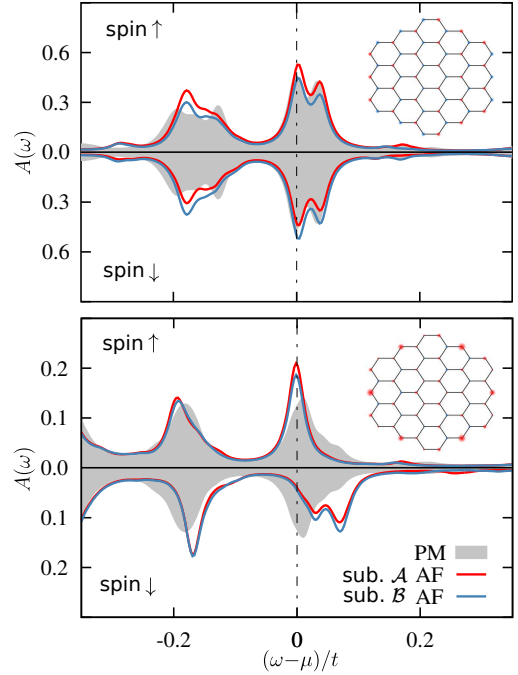


FIG. 7. (Color online) As in Fig. 6 but for $\delta = 3$, showing a FM alignment of the C_e^2 magnetic moments below T_c .

In the FI state all the inequivalent C_e^2 spins are aligned FM, although they are not equal in size due to the breaking of the sublattice symmetry. The trend of the data at low T suggests that the sublattice asymmetry could possibly disappear in the limit $T \rightarrow 0$. Away from the transition, the properties of the ZGNF are nearly independent on T up to a sharp drop above T_{room} . A similar behavior is found at $\delta = 3$ (fourth panel in Fig. 5). We can estimate the transition temperature to $T_c \approx 100$ K, which results to be lower than the one for $\delta = 2$. Interestingly, the effect in the bulk atoms in the ZGNF is weaker, although a clear discontinuity in the T dependence of the local magnetic moment can be observed for $\delta = 2$ and $\delta = 3$ (not shown).

At $\delta \neq 0$ the magnetization also displays a hysteretic behavior. The hysteresis is evident especially for $\delta = 2$ and $\delta = 3$, where it extends over a wide range of T and indicates a coexistence of short-range AF and FM orders. We notice that both the local magnetic moments $\langle S_i^z \rangle$ decrease upon doping. While this is expected within DMFT, it is instead absent in reference $T = 0$ DFT calculations, where the spin density at the edges is the same in both the AF and the FI states.¹⁴

It is interesting to relate the changes in the local magnetic moments at the ZZ edges across the AF-to-FI transition, with the changes in the low-energy excitation in the spectral functions. To this end, we focus on the edge C_e^2 atoms of sublattices \mathcal{A} and \mathcal{B} . The corresponding local spin-resolved spectral functions $A(\omega)$ in the PM and the magnetic (AF or FI) states are shown in Figs. 6 and 7 at $\delta = 2$ and $\delta = 3$, respectively. A common feature

of doped ZGNFs is the metallic character of the spectrum due to a redistribution of spectral weight in the site-resolved $A(\omega)$ with respect to half-filling (compare with Fig. 3). We observe a resonance at the Fermi level, associated with the delocalization of the electrodedoped charge carriers on the lattice. The low-energy coherent excitations at $\delta \neq 0$ coexist with the incoherent high-energy excitations (Hubbard bands) related to the formation of the fluctuating local moment due to the Coulomb interaction. In the magnetic state above $T_c(\delta)$ the analysis of the spectral functions in (the upper panels of) Figs. 6 and 7 clearly indicates the AF alignment of the C_e^2 atoms in the different sublattices. Below T_c (lower panels) a redistribution of low-energy spectral weight splits the spin- \uparrow and spin- \downarrow spectral functions with respect to the Fermi level, showing a tendency toward an insulating state. The splitting is the same for sublattice \mathcal{A} and \mathcal{B} . As a consequence the local magnetic moments of the edge C_e^2 atoms in the two sublattices are aligned FM. For $\delta = 2$ the sublattice asymmetry is evident while for $\delta = 3$ is minimal. The spatial distribution of the magnetic moments above and below T_c , and the corresponding change of the magnetic pattern for both values of δ are shown in the respective insets.

In order to understand the nature of the magnetic correlations at the ZZ edges we analyze the spatial distributions of the holes upon doping. In the upper panel of Fig. 8 we show the local hole density for the bulk C_b^1 and edge C_e^2 atoms as a function of the average electron density $\langle n \rangle$ in the ZGNF. The holes are found to be localized mostly at the ZZ edges, and the ratio between the hole concentration at the edge and in the bulk increases with doping. However, the average hole concentration on the lattice obtained within DMFT is less heterogeneous than in reference DFT calculations¹⁴ due to the effects of the hole-hole repulsion at the edges. The hole concentration in Fig. 8 is shown for $T/t = 0.005$ ($T \approx 80$ K), which is below $T_c(\delta)$ for all $\delta \neq 0$, but the spatial distribution of the holes on the lattice is very weakly dependent on T (not shown). We also find that there is no sizable redistribution of the holes on the lattice between the PM and the magnetically ordered states, except for a slight asymmetry due to the sublattice symmetry breaking in the FI state. In the other two panels of Fig. 8, we show the evolution with doping of the average fluctuating local moment $\langle p \rangle = \frac{1}{N} \sum_i \langle p_i \rangle$ in relation with the magnetization m and m_{st} in the ordered state. Upon ordering magnetically, the value of $\langle p \rangle$ increases due to the reduction of the double occupations. At half-filling this corresponds to the gain of potential energy shown in the inset of Fig. 2. We note that $\langle p \rangle$ is weakly dependent on doping. If we compare it with the value $\langle p \rangle$ in the uncorrelated (free) and the fully localized cases, where the local double occupations are $\langle n_{i\uparrow} n_{i\downarrow} \rangle = 0.25$ and $\langle n_{i\uparrow} n_{i\downarrow} \rangle = 0$, respectively. we can conclude that $\langle p \rangle$ gets closer to the localized limit upon doping. At the same time the magnetization m_{st} is strongly suppressed in favor of a uncompensated magnetic moment m as FM

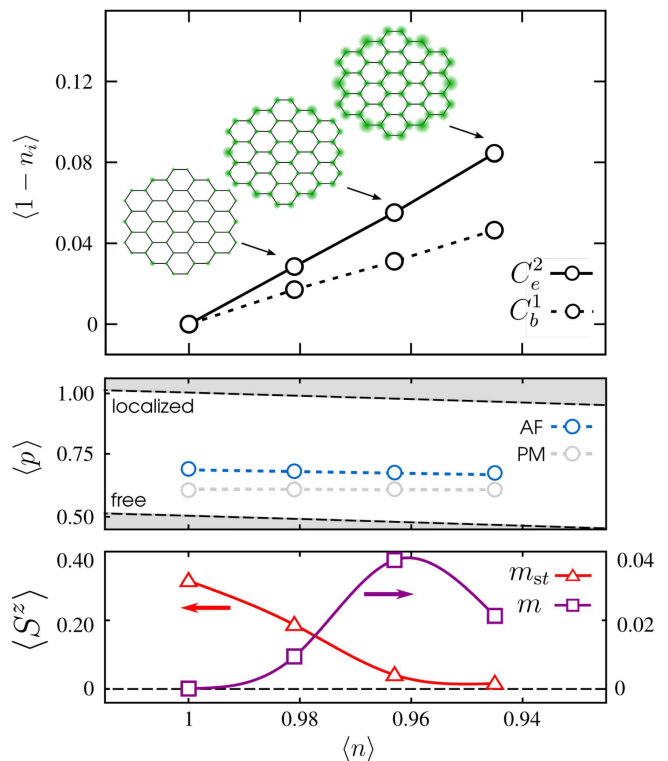


FIG. 8. (Color online) Distribution and influence of the doped holes as a function of the average electron density in the ZGNF $\langle n \rangle$ at $U/t = 3.75$ and $T \approx 80$ K. [Upper panel] Local hole density $\langle 1 - n_i \rangle$ for the bulk C_b^1 and the edge C_e^2 atoms in the PM state. The spatial distribution of the holes in the ZGNF is shown in the insets. [Middle panel] The average fluctuating local moment $\langle p \rangle$. The dashed lines separating the shaded area correspond to the free and fully localized limits (see text for the details). [Lower panel] Absolute value of the net magnetic moment m and staggered magnetization m_{st} .

correlations tend to align the magnetic moment at the ZZ edges. The net magnetic moment as a function of doping $m(\delta)$ displays a dome shape, peaked at an optimal value of $\delta \approx 2$, which develops upon lowering T . Within the usual DMFT picture, the presence of a sizable *preformed* local moment while the magnetic order is capped by a lower coherence energy scale, would indicate the realization of a strong-coupling scenario.^{47,48} This suggests a crossover from weak- to strong-coupling magnetism in ZGNF upon doping away from half-filling. Based on these observations we can argue that the delocalized holes mediate an effective magnetic exchange interaction, which is dynamically generated between the magnetic moments localized at the edges. This mechanism ultimately leads to the change of the magnetic structure in the doped ZGNF. This highly non-trivial physics can be indeed captured by DMFT because it is able to describe both the coherent and the incoherent excitations as well as their interplay. Evidence in support of this claim is presented in Sec. III C, where we evaluate the effective magnetic exchange interaction.

TABLE I. Relevant effective magnetic interaction parameters J_{ij}/t [10^{-4}]. In the upper table the long-range interactions J_1 , J_2 , J_3 denote exchange between edge C_e^2 atoms belonging to neighboring, next-nearest neighboring, and opposite edges of the ZGNF, respectively. While J_1 and J_3 always connect C_e^2 atoms on different sublattices, J_2 connects C_e^2 atoms on the same sublattice, and assumes different values if the sublattice symmetry is broken. In the lower table the NN interactions denote exchange between C_b^1 pairs, C_e^1 pairs, or C_b^4 - C_e^2 pairs. The latter assumes different values if the sublattice symmetry is broken. The above magnetic exchanges are also indicated graphically on the ZGNF in Fig. 9, for the sake of clarity.

	$T/t = 0.005$ ($T \approx 80$ K)				$T/t = 0.010$ ($T \approx 160$ K)			
	J_1^{AB}	J_2^{AA}	J_2^{BB}	J_3^{AB}	J_1^{AB}	J_2^{AA}	J_2^{BB}	J_3^{AB}
$\delta = 0$	0.38(5)	0.01(6)	0.01(6)	0.04(5)	0.38(4)	0.01(6)	0.01(6)	0.04(5)
$\delta = 1$	-0.34(9)	0.26(5)	0.17(1)	-1.08(5)	-0.21(9)	0.14(3)	0.14(5)	-0.75(7)
$\delta = 2$	0.05(9)	0.02(4)	0.02(5)	0.09(1)	-0.05(0)	0.00(6)	0.01(8)	-0.08(6)
$\delta = 3$	0.03(9)	-0.01(1)	0.01(5)	-0.00(6)	-0.01(4)	-0.00(1)	-0.00(1)	-0.00(1)

	$J_{NN}^{AB} C_b^1-C_b^1$	$J_{NN}^{AB} C_e^1-C_e^1$	$J_{NN}^{AB} C_b^4-C_e^2$	$J_{NN}^{BA} C_b^4-C_e^2$	$J_{NN}^{AB} C_b^1-C_b^1$	$J_{NN}^{AB} C_e^1-C_e^1$	$J_{NN}^{AB} C_b^4-C_e^2$	$J_{NN}^{BA} C_b^4-C_e^2$
$\delta = 0$	1.00(4)	5.52(4)	2.70(2)	2.70(9)	1.01(3)	5.47(1)	2.68(4)	2.69(3)
$\delta = 1$	0.26(2)	2.05(4)	0.77(0)	1.03(1)	0.27(0)	2.01(2)	0.91(6)	0.91(0)
$\delta = 2$	0.00(3)	0.02(5)	0.22(9)	-0.08(1)	0.02(6)	0.26(8)	0.13(7)	0.07(6)
$\delta = 3$	-0.00(1)	-0.00(6)	-0.02(0)	0.04(0)	0.00(7)	0.07(2)	0.02(7)	0.03(1)

C. Effective magnetic interaction

In the following we analyze the effective magnetic interactions generated by the interplay of the local repulsion U and the delocalization of electrons and holes in the ZGNF, which we argue to be the mechanism behind the stabilization of the FI state. Within the local self-energy approximation (as in DMFT), an estimate of the effective magnetic exchange interaction parameters J_{ij} can be obtained, following Katsnelson and Lichtenstein,⁶¹ as

$$J_{ij} = - \int_{-\infty}^{\infty} d\omega \Sigma_i^s(\omega) G_{ij}^\uparrow(\omega) \Sigma_j^s(\omega) G_{ji}^\downarrow(\omega) f(\omega), \quad (4)$$

where $f(\omega) = (e^{\beta(\omega-\mu)} + 1)^{-1}$ is the Fermi distribution function at the inverse temperature $\beta = 1/T$, while $\Sigma_i^s = (\Sigma_i^\uparrow - \Sigma_i^\downarrow)/2$ is the asymmetric spin combination of the local (dynamical) self-energy, and G_{ij}^σ is the real-space non-local Green's function connecting sites i and j , with spin σ . Diagrammatically, the effective exchange J_{ij} can be thought as the frequency convolution of the bubble term χ_{ij}^0 of the non-local susceptibility, with the non-local Green's function as the fermionic lines of the bubble and Σ_i^s playing the role of the local vertex. Let us stress that the coupling J_{ij} is zero in the PM state (where $\Sigma_i^\uparrow = \Sigma_i^\downarrow$) and it should not be interpreted as the magnetic coupling of an effective spin lattice Hamiltonian (e.g., of the Heisenberg model), as it carries a temperature and doping dependence through both the Green's function and self-energy. Rather, Eq. (4) resembles the typical expression^{21,25} used to evaluate the RKKY exchange coupling between magnetic adatoms: $J_{\text{RKKY}} \propto J^2 \chi_{ij}^0$, where J couples the impurity spin with the spin density on the substrate, and χ_{ij}^0 is the static spin susceptibility of the conduction electrons, which me-

diates the effective magnetic interaction. In analogy, we have that Σ_i^s is associated with the presence of localized magnetic moments and the effective exchange between them is mediated by the doped holes delocalized on the lattice.

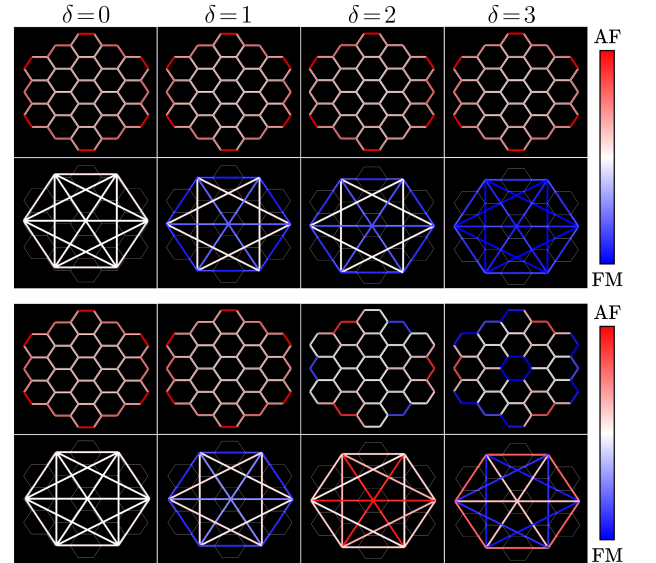


FIG. 9. (Color online) Effective magnetic exchange J_{ij} between all NN pairs and edge C_e^2 atom pairs for different dopings. The color and the intensity of the links denote the nature and the strength of the magnetic interaction: from AF (red/light grey) to FM (blue/dark grey). The data are normalized to the strongest J_{ij} for a better visibility, while the numerical values of the couplings are given in Tab. I as a reference. [Upper panels] AF state, at $T/t = 0.010$ ($T \approx 80$ K). [Lower panels] FI state, at $T/t = 0.005$ ($T \approx 160$ K).

The expression for J_{ij} in Eq. (4) yields the effective magnetic exchange for any pair (i, j) in the ZGNF. However, in order to highlight the microscopic mechanism behind the AF-to-FI magnetic transition, we focus on the magnetic exchange parameters between all NN atom pairs and all edge C_e^2 atom pairs. In Fig. 9 we show a graphical representation on the ZGNF of the values obtained for relevant magnetic exchange parameters J_{ij} . We show data as a function of doping and for two values of temperature, $T/t = 0.010$ ($T \approx 160$ K) and $T/t = 0.005$ ($T \approx 80$ K), which are representative of the high- T (AF) and low- T (FI) magnetic states discussed above. At half-filling, we find all magnetic interactions $J_{ij} > 0$ (i.e., AF in nature). The short-range, and in particular the NN interactions J_{NN} are stronger at the edges with respect to the bulk. The values of J_{ij} are rapidly suppressed with distance $|i - j|$, and in particular long-range interactions between different edges are negligibly weak with respect to J_{NN} within a given edge. The magnetic properties at half-filling are weakly dependent on T (below T_N) and this is reflected also in the magnetic couplings. At finite doping and above T_c we find $J_{NN} > 0$ and quantitatively similar to the ones at $\delta = 0$ for all values of doping. However, the presence of delocalized charge carriers mediate sizable long-range magnetic interactions. Some of the long-range interactions connecting edge C_e^2 atoms, indicated as J_1 , J_2 , and J_3 in Tab. I, are found to be negative (i.e., FM in nature) at finite doping. Eventually, the presence of $J_{ij} < 0$ drives the onset of the FI state as $T \rightarrow T_c(\delta)$. Interest-

ingly, below $T_c(\delta)$ the change in the magnetic structure at $\delta \neq 0$ is reflected also in a change of the effective exchange interactions. The results are clearer for $\delta = 2$ and $\delta = 3$, where an exact correspondence can be found between the J_{NN} shown in Fig. 9 and the relative orientation of the corresponding pair of magnetic moments shown, e.g., in the insets of Figs. 6 and 7, respectively. The behavior of long-range interactions is less obvious and better illustrated in Fig. 10, in which we compare the doping dependence of both representative J_{NN} and the J_{1-3} magnetic exchange interactions above and below T_c . In general J_{NN} become weaker upon doping, with some of them (in particular at the ZZ edges) becoming FM at $\delta = 2$ and $\delta = 3$ below T_c . Instead, long-range interactions are enhanced at $\delta = 1$ with respect to the half-filling case, but are suppressed upon further increasing the doping. The interaction J_1 and J_3 , that connect edge C_e^2 atoms of different sublattices, are usually larger than J_2 and display an oscillatory behavior, changing sign as a function of doping. In particular, the FM nature of $J_1 < 0$ and $J_3 < 0$ above T_c reveals the tendency of magnetic moments at the ZZ edges to align FM, and can be interpreted as the microscopic mechanism driving the system across the AF-to-FI transition. Below T_c , we find $J_{1-3} > 0$ for $\delta = 2$ and $\delta = 3$ and we interpret it as a signature of the competition between the AF and the FI states. Evidence for the coexistence and the cooperation of AF and FM correlations in determining the magnetic state of doped triangular and linear chain ZGNFs was already discussed by Chacko *et al.*²⁰ within exact diagonalization calculations. This hints at the generality of the above scenario in graphene nanostructures, which not limited to a particular shape, but seems to be a general feature related to the presence of ZZ edges. Note, however, that the values of the FM J_{ij} couplings extracted in the calculations are relatively weak compared to the AF J_{NN} and the temperature scale T_c at which the FI magnetic order sets in. This suggests that also the geometry of the ZGNF plays an important role, assisting the exchange couplings in the formation of the FI state.

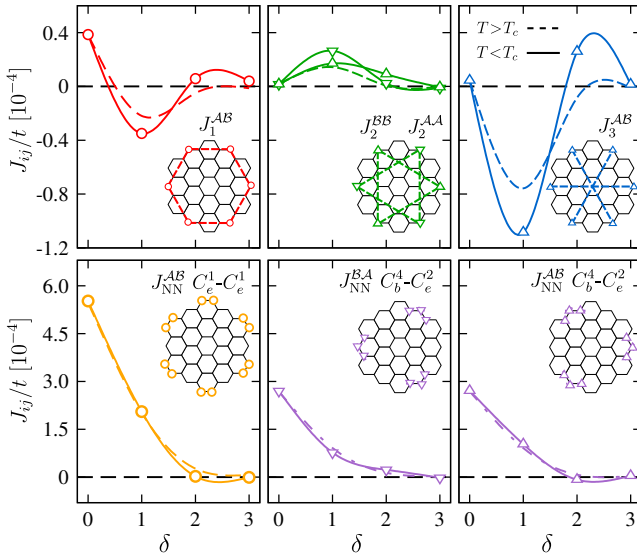


FIG. 10. (Color online) Effective parameters for relevant magnetic interactions J_{ij} as a function of doping δ . The dashed and solid lines (guides to the eye) with open symbols correspond to $T/t = 0.010$ ($T > T_c$) and $T/t = 0.005$ ($T < T_c$), respectively. [Upper panels] Long-range interactions J_1 , J_2 , J_3 . [Lower panels] J_{NN} interactions between C_e^1 - C_e^1 and C_b^4 - C_e^2 pairs. The corresponding values are given in Tab. I.

IV. SUMMARY AND OUTLOOK

In this work we investigated the interplay between charge and spin degrees of freedom in the magnetic properties of a doped ZGNF within the framework of DMFT. At half-filling we analyze the onset of magnetism as a function of the local interaction U . We identify a dichotomy between bulk and edge C atoms, which persist from weak- to strong-coupling. Above a threshold value of U , the ground state of the ZGNF is in a fully-compensated AF state. The analysis of the energy balance within DMFT suggests that, for realistic values of the interaction, at half-filling the AF state is stabilized by a weak-coupling mechanism. The results obtained are in qualitative agreement with static-MFT and DFT calculations, but show that quantum fluctuations suppress

AF with respect to mean-field approximations.

Upon introducing charge carriers we observe the melting of the AF state. Below a doping-dependent ordering temperature $T_c(\delta)$ it is possible to stabilize a short-range FI order, in which the magnetic moments at the ZZ edges are aligned FM. In the FI state the ZGNF displays a net ferromagnetic moment which coexists with a finite staggered magnetization. We interpret the change in the magnetic configuration in terms of an effective magnetic exchange between the ordered spins, mediated by the charge carriers localized in the proximity of the edges.

The possibility of driving FM correlations upon doping was already discussed in the framework of DFT¹⁴ and exact diagonalization.²⁰ The overall agreement with these studies indicates that a reasonable description of the magnetic phases can already be obtained relying on a mean-field description of long-range correlations. In this framework, DMFT has allowed us to accurately capture the interplay between the incoherent excitations that form the fluctuating local moment and the coherent low-energy excitations that screen this local moment on longer time scales and mediate the magnetic exchange which stabilize the ordered state. Moreover, the possibility of describing both the temperature and doping dependence of the effective exchange couplings sheds some light on the onset of the FI short-range order and the strong competition between AF- and FM-correlations in ZGNFs.

Evidently, any change in the magnetism and in the low-energy spectral properties will have important consequences on the transport through ZGNFs. Hence, the above analysis indicate the electrostatic control of the magnetization of doped ZGNF as a promising route towards the future conception and realization of carbon based spintronic devices.

ACKNOWLEDGMENTS

We acknowledge valuable discussions with R. Drost, D. Prezzi, and Z. Zhong. We are grateful to G. Sangiovanni for helpful discussions in several stages of this work, and to M. Pickem who provided a benchmark for the static-MFT results. We acknowledge financial support from the Austrian Science Fund (FWF) through the Erwin Schrödinger fellowship J3890-N36 (AV), through project I-610-N16 (AT), and the SFB ViCoM (AT, AV, KH), as well as the European Research Council under the European Union's Seventh Framework Program FP7/ERC through grant agreement n. 306447 (KH, AV), n. 240524 (MC, AA, AV), and n. 280555 (AA).

Appendix A: Details of the numerical simulations

In the following we discuss the technical details of the magnetic real-space DMFT calculations and the annealing procedure used to obtain the temperature evolution

of the magnetic properties of the ZGNF.

The auxiliary AIMs of the real-space DMFT algorithm are solved with a Lanczos exact diagonalization impurity solver^{62,63} which is able to accurately describe the physics both at $T = 0$ and at finite T . We employ a typical discretization of the Hilbert space of $n_s = 1 + n_b = 9$ sites, with n_b being the number of bath sites connected to the impurity. In specific cases we also performed calculations up to $n_s = 12$ sites, finding no qualitative difference in the physical observables. The reliability of the finite temperature results obtained with Lanczos exact diagonalization impurity solver was tested against continuous-time Quantum Monte Carlo impurity solver implemented in the w2dynamics package,⁶⁴ showing quantitative agreement in the physical observables.

In order to get a magnetic solution within real-space DMFT, we lift the local $SU(2)$ spin rotational symmetry of each auxiliary AIM. The symmetry is manually broken at the beginning of the self-consistency cycle by applying a symmetry-breaking field $\eta_{i\sigma}$ to the spin-dependent DMFT bath $\mathcal{G}_{0i\sigma}(\omega)$. In the case of a AF state, symmetry-breaking field takes the form

$$\eta_{i\sigma} = \begin{cases} \eta(\delta_{\sigma\uparrow} - \delta_{\sigma\downarrow}), & \text{if } i \in \mathcal{A} \\ \eta(\delta_{\sigma\downarrow} - \delta_{\sigma\uparrow}), & \text{if } i \in \mathcal{B} \end{cases} \quad (\text{A1})$$

where we set the parameter $\eta = 0.05t > 0$. The field in Eq. (A1) corresponds to a staggered perturbation with the same symmetry of the fully-compensated AF state.

At half-filling the system is unstable toward AF and the convergence of the DMFT self-consistency is smooth down to $T = 0$. At finite doping $\delta \neq 0$, besides the solution of the inhomogeneous real-space DMFT equations, one also needs to determine the chemical potential $\mu(n)$ corresponding to electron concentration $n = \sum_{i\sigma} \langle n_{i\sigma} \rangle$. The search for $\mu(n)$ involves a complex root-finding within the self-consistent procedure, which makes the convergence of the DMFT self-consistency numerically unstable for arbitrary values of T and δ . The difficulty of the root-finding is also enhanced due to the discreteness of the energy spectrum for a nanoscopic system. However, motivated by physical observations, it is possible to obtain a reliable self-consistent solution of the DMFT equations in a wide range of T and δ by following an annealing procedure. Indeed, one can notice that at high- T , AF short-range magnetic correlations are dominant, as evident by the values of the effective magnetic exchange J_{ij} shown in Tab. I. The AF correlations stabilize a fully-compensated AF state, also at $\delta \neq 0$. A staggered spatial order of the magnetic moments can be easily obtained at high- T with the natural choice in Eq. (A1) for $\eta_{i\sigma}$, mainly for two reasons: (i) the magnetic ground state displays a spatial distribution of the magnetic moments that closely resembles the initial state given by the symmetry-breaking field $\eta_{i\sigma}$; (ii) the temperature broadening soothes the complexity of the root-finding in the case of a discrete energy spectrum. Once a high- T calculation is converged, the chemical potential μ , the

spin-dependent Weiss fields $\mathcal{G}_{0i\sigma}(\omega)$, and the list of the L nczos states for each inequivalent atom are used as an input for the calculation at lower T . As the input Weiss field for the next calculation is already symmetry-broken, the annealing procedure in continued *without* imposing a

symmetry-breaking field $\eta \neq 0$ with any specific spatial structure. This way, we observe a *spontaneous* transition toward the FI state in the low- T regime. In analogy, a reverse annealing procedure was followed starting from a converged low- T calculation. This allowed to reveal the hysteretic behavior of the magnetic moments at $\delta \neq 0$.

-
- ¹ I. Snook and A. Barnard. Graphene Nano-Flakes and Nano-Dots: Theory, Experiment and Applications, Physics and Applications of Graphene - Theory, Dr. Sergey Mikhailov (Ed.), InTech, (2011). DOI: 10.5772/15541.
 - ² Y.-W. Son, M. L. Cohen, and S. G. Louie, Phys. Rev. Lett. **97**, 216803 (2006).
 - ³ Y. Wang, Y. Huang, Y. Song, X. Zhang, Y. Ma, J. Liang, and Y. Chen, Nano Lett. **9**, 220 (2009).
 - ⁴ H. S. S. Ramakrishna Matte, K. S. Subrahmanyam, C. N. R. Rao, J. Phys. Chem. C **113**, 9982 (2009).
 - ⁵ L. Chen, L. Guo, Z. Li, H. Zhang, J. Lin, J. Huang, S. Jin, and X., Chen, Sci. Rep. **3**, 2599 (2013).
 - ⁶ G. Z. Magda, X. Jin, I. Hagym si, P. Vancs , Z. Osv th, P. Nemes-Incze, C. Hwang, L. P. Bir , and L. Tapaszt , Nature **514**, 608 (2014).
 - ⁷ R. Drost, S. Kezilebieke, M. M. Ervasti, S. K. H m l inen, F. Schulz, A. Harju, and P. Liljeroth, Sci. Rep. **5**, 16741 (2015).
 - ⁸ R. Drost, A. Uppstu, F. Schulz, S. K. H m l inen, M. Ervasti, A. Harju, and P. Liljeroth, Nano Lett. **14**, 5128 (2014).
 - ⁹ I. A. Verzhbitskiy, M. De Corato, A. Ruini, E. Molinari, A. Narita, Y. Hu, M. G. Schwab, M. Bruna, D. Yoon, S. Milana, X. Feng, K. M llen, A. C. Ferrari, C. Casiraghi, and D. Prezzi, Nano Lett. **6**, 3442 (2016).
 - ¹⁰ Y.-W. Son, M. L. Cohen, and S. G. Louie, Nature **444**, 347 (2006).
 - ¹¹ W. L. Wang, S. Meng, and E. Kaxiras, Nano Lett. **8**, 241 (2008).
 - ¹² J. Kang, F. Wu, and J. Li, J. Appl. Phys. **112**, 104328 (2012).
 - ¹³ W. Sheng, Z. Y. Ning, Z. Q. Yang, and H. Guo, Nanotechnology **21** 385201 (2010).
 - ¹⁴ M. Kabir and T. Saha-Dasgupta, Phys. Rev. B **90**, 035403 (2014).
 - ¹⁵ J. Fernandez-Rossier and J. J. Palacios, Phys. Rev. Lett. **99**, 177204 (2007).
 - ¹⁶ W. L. Wang, O. V. Yazyev, S. Meng, and E. Kaxiras, Phys. Rev. Lett. **102**, 157201 (2009).
 - ¹⁷ Y. Zhou, Z. Wang, P. Yang, and F. Gao, J. Phys. Chem. C **116**, 7581 (2012).
 - ¹⁸ F. Zou, L. Zhu, and K. Yao, Sci. Rep. **5**, 15966 (2015).
 - ¹⁹ W. Zhang, Sci. Rep. **4**, 6320 (2014).
 - ²⁰ S. Chacko, D. Nafday, D. G. Kanhere, and T. Saha-Dasgupta, Phys. Rev. B **90**, 155433 (2014).
 - ²¹ A. M. Black-Schaffer, Phys. Rev. B **81** 205416 (2010).
 - ²² Karol Sza owski, Phys. Rev. B **84**, 205409 (2011).
 - ²³ Karol Sza owski, Phys. Rev. B **90**, 085410 (2014).
 - ²⁴ F. M. Hu, T. Ma, H.-Q. Lin, and J. E. Gubernatis, Phys. Rev. B **84**, 075414 (2011).
 - ²⁵ B. Uchoa, T. G. Rappoport, and A. H. Castro Neto, Phys. Rev. Lett. **106**, 016801 (2011).
 - ²⁶ H. Feldner, Z. Y. Meng, A. Honecker, D. Cabra, S. Wessel, and F. F. Assaad, Phys. Rev. B **81**, 115416 (2010).
 - ²⁷ Z. Y. Meng, T. C. Lang, F. F. Assaad, S. Wessel, and A. Honecker, Phys. Rev. Lett. **106** 226401 (2011).
 - ²⁸ S. Dutta and K. Wakabayashi, Sci. Rep. **2**, 519 (2012).
 - ²⁹ A. Georges, G. Kotliar, W. Krauth and M. Rozenberg, Rev. Mod. Phys. **68**, 13 (1996).
 - ³⁰ A. Kretinin, G. L. Yu, R. Jalil, Y. Cao, F. Withers, A. Mishchenko, M. I. Katsnelson, K. S. Novoselov, A. K. Geim, and F. Guinea, Phys. Rev. B **88**, 165427 (2013).
 - ³¹ T. O. Wehling, E. S s lo lu, C. Friedrich, A. I. Lichtenstein, M. I. Katsnelson, and S. Bl gel, Phys. Rev. Lett. **106**, 236805 (2011).
 - ³² M. Sch ler, M. R sner, T. O. Wehling, A. I. Lichtenstein, and M. I. Katsnelson, Phys. Rev. Lett. **111**, 036601 (2013).
 - ³³ M. Potthoff and W. Nolting, Phys. Rev. B **59**, 2549 (1999).
 - ³⁴ S. Florens, Phys. Rev. Lett. **99**, 046402 (2007).
 - ³⁵ M. Snoek, I. Titvinidze, C. T ke, K. Byczuk, and W. Hofstetter, New J. Phys. **10**, 093008 (2008).
 - ³⁶ I. Titvinidze, A. Schwabe, N. R ther, and M. Potthoff, Phys. Rev. B **86**, 075141 (2012).
 - ³⁷ A. Valli, G. Sangiovanni, O. Gunnarsson, A. Toschi, and K. Held, Phys. Rev. Lett. **104**, 246402 (2010).
 - ³⁸ D. Jacob, K. Haule, and G. Kotliar, Phys. Rev. B **82**, 195115 (2010).
 - ³⁹ A. Valli, G. Sangiovanni, A. Toschi, and K. Held, Phys. Rev. B **86**, 115418 (2012).
 - ⁴⁰ H. Das, G. Sangiovanni, A. Valli, K. Held, and T. Saha-Dasgupta, Phys. Rev. Lett. **107**, 197202 (2011).
 - ⁴¹ A. Valli, H. Das, G. Sangiovanni, T. Saha-Dasgupta, and K. Held, Phys. Rev. B **92**, 115143 (2015).
 - ⁴² A. Valli, T. Sch fer, P. Thunstr m, G. Rohringer, S. Andergassen, G. Sangiovanni, K. Held, and A. Toschi, Phys. Rev. B **91**, 115115 (2015).
 - ⁴³ A. Toschi, A. A. Katanin, and K. Held, Phys. Rev. B **75**, 045118 (2007).
 - ⁴⁴ G. Rohringer, A. Valli, and A. Toschi, Phys. Rev. B **86**, 125114 (2012).
 - ⁴⁵ K. A. Ritter and J. W. Lyding, Nature Materials **8**, 235 (2009).
 - ⁴⁶ W. Hu, L. Lin, C. Yang, and J. Yang J. Chem. Phys. **141**, 214704 (2014).
 - ⁴⁷ A. Toschi, M. Capone, and C. Castellani, Phys. Rev. B **72**, 235118 (2005).
 - ⁴⁸ C. Taranto, G. Sangiovanni, K. Held, M. Capone, A. Georges, and A. Toschi, Phys. Rev. B **85**, 085124 (2012).
 - ⁴⁹ A. Tagliavini, M. Capone, and A. Toschi, arXiv:1604.08882 (2016).
 - ⁵⁰ G. Rohringer and A. Toschi, arXiv:1604.08748 (2016).
 - ⁵¹ S. Sorella and E. Tosatti, Europhys. Lett. **19**, 699 (1992).
 - ⁵² S. Sorella, Y. Otsuka, S. Yunoki, Sci. Rep. **2**, 992 (2012).
 - ⁵³ H.-S. Tao, Y.-H. Chen, H. F. Lin, H. D. Liu, and

- W. M. Liu, Scientific Reports **4**, 5367 (2014).
- ⁵⁴ S. Arya, P. V. Sriluckshmy, S. R. Hassan, and A.-M. S. Tremblay, Phys. Rev. B **92**, 0451111 (2015).
- ⁵⁵ M. Sentef, J. Kuneš, P. Werner, and A. P. Kampf, Phys. Rev. B **80**, 155116 (2009).
- ⁵⁶ A. Amaricci, A. Privitera, and M. Capone, Phys. Rev. A **89**, 053604 (2014).
- ⁵⁷ With a particle-hole symmetric Hamiltonian the physics does not change upon electron doping. However, this is no longer true if structural relaxations for the non-passivated ZGNF are considered.
- ⁵⁸ H. S. Moon, J. M. Yun, K. H. Kim, S. S. Jangd, and S. G. Lee, RSC Adv., **6**, 39587 (2016).
- ⁵⁹ G. Rohringer, A. Toschi, A. Katanin, and K. Held, Phys. Rev. Lett. **107**, 256402 (2011).
- ⁶⁰ D. Hirschmeier, H. Hafermann, E. Gull, A. I. Lichtenstein, and A. E. Antipov, Phys. Rev. B **92**, 144409 (2015).
- ⁶¹ M. I.Katsnelson and A. I. Lichtenstein, Phys. Rev. B **61**, 8906 (2000).
- ⁶² M. Caffarel and W. Krauth, Phys. Rev. Lett. **72**, 1545 (1994).
- ⁶³ M. Capone, L. de' Medici, and A. Georges, Phys. Rev. B **76**, 245116 (2007).
- ⁶⁴ N. Parragh, A. Toschi, K. Held, and G. Sangiovanni, Phys. Rev. B **86**, 155158 (2012).